NANO LETTERS

pubs.acs.org/NanoLett Letter

Size-Coded Hydrogel Microbeads for Extraction-Free Serum Multi-miRNAs Quantifications with Machine-Learning-Aided Lung Cancer Subtypes Classification

Dayu Chen,[#] Yingfei Wang,[#] Ying Wei, Zhenda Lu, Huangxian Ju, Feng Yan,* and Ying Liu*

Cite This: *Nano Lett.* 2025, 25, 453−460 Read Online

ABSTRACT: Classifying lung cancer subtypes, which are characterized by multi-microRNAs (miRNAs) upregulation, is important for therapy and prognosis evaluation. Liquid biopsy is a promising approach, but the pretreatment of RNA extraction is labor-intensive and impairs accuracy. Here we develop size-coded hydrogel microbeads for extraction-free quantification of miR-21, miR-205, and miR-375 directly from serum. The hydrogel microbead is immobilized with an miRNA capture probe, which well retains target miRNA and provides good nonfouling capability for nonspecific biomolecules in serum. The porous structure of microbeads allows efficient DNA cascade amplification reaction and generates a fluorescence signal. The microbeads are clustered into three groups according to size via flow cytometry sorting, and the group fluorescence is integrated for the corresponding miRNA quantification. With machine-learning-assisted data analysis, it achieves good lung cancer diagnosis accuracy and 80% accuracy for subtype classification for 108 serum samples, including lung cancer patients and healthy controls.

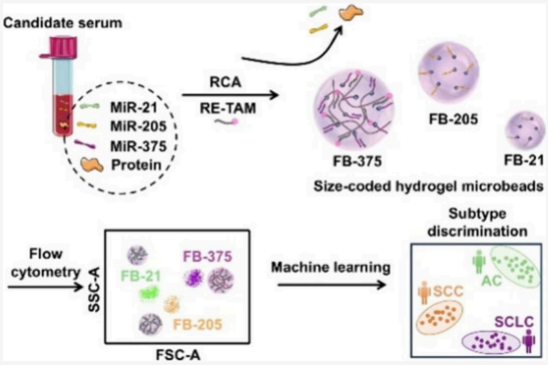

KEYWORDS: *cancer subtypes classification, miRNA, hydrogel microbeads, extraction-free, machine-learning*

Lung cancer is one of the most frequently diagnosed cancers and the leading cause of cancer-related death worldwide,[1,2] and it is divided into non-small-cell lung cancer (NSCLC, 85%) which includes adenocarcinoma (AC) and squamous-cell carcinoma (SCC) subtypes, and small-cell lung cancer (SCLC, 15%).[3,4] Considering their unique disease biology, classification of lung cancer subtypes in early diagnosis is very important, which guides the treatment plan chosen and prognosis evaluation.

The current gold standard for lung cancer subtypes classification is histopathological examinations including morphology analysis and immunohistochemical staining (IHC).[5,6] However, it requires invasive sampling and time-costing operation processes. Heterogeneous tumor internal situations and different sampling positions may also impair the assessment accuracy. As a noninvasive detection method, liquid biopsy is a promising substitute that quantifies disease characteristic biomarkers via blood analysis.[7] The recent advances in disease biomarker identification and machine-learning-assisted data analysis further improve assessment accuracy.

MicroRNAs (MiRNAs) play important roles in biological process and have become early cancer diagnostic biomarkers with clinical application prospect.[8,9] Lung cancer subtypes are characterized by different types and expression levels of miRNAs. For example, miRNA-205 is mainly upregulated in NSCLC, especially SCC.[10−12] The different expression levels of miR-205 and miRNA-21 (miR-21) allow histotype classification between AC and SCC.[13] SCLC[14] and AC[15] have obviously upregulated miRNA-375 expression, while SCC has comparatively lower expression level.[16] Therefore, quantifying multiple miRNAs is important for lung cancer subtypes classification.[17] Considering low miRNA concentrations (pM) and the complex environment of serum, producing and distinguishing multiple miRNA signals remains a great challenge.[18,19] Current multi-miRNAs quantification techniques include microarray,[20] microfluidics,[21,22] or direct sequencing.[23,24] However, these techniques all require a pretreatment process of RNA extraction from bodily fluids, which is labor-intensive and may influence detection accuracy due to the loss and degradation of target miRNAs.[25] Extraction-free detection of a scarce amount of miRNAs directly from bodily fluid is necessary for successful clinical translation, but appropriate techniques are still lacking.[26,27]

Received: October 20, 2024
Revised: December 10, 2024
Accepted: December 12, 2024
Published: December 16, 2024

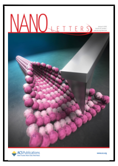

https://doi.org/10.1021/acs.nanolett.4c05233
Nano Lett. 2025, 25, 453−460

Scheme 1. Schematic Illustrations[a]

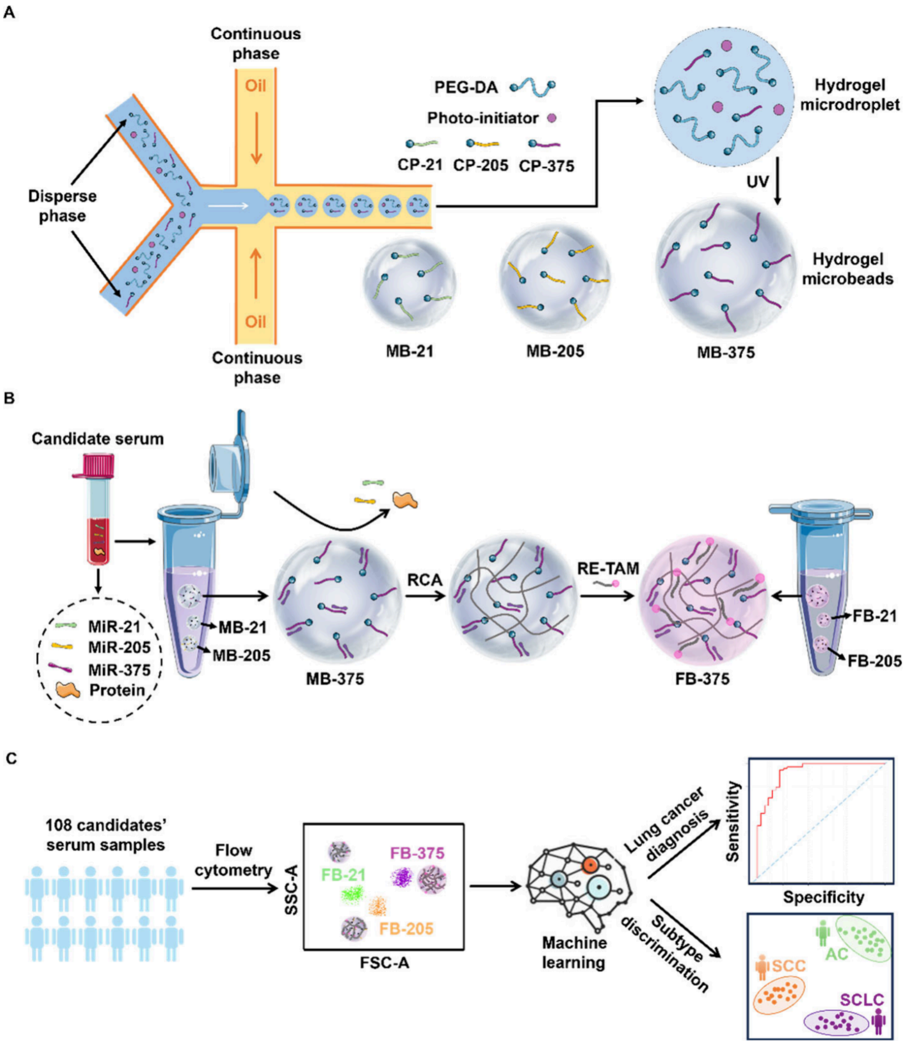

[a](A) Size-coded hydrogel microbeads MB-21, MB-205, MB-375 synthesis. (B) Capture of miR-21, miR-205, miR-375 directly from serum without extraction process and fluorescence signal amplification in microbeads. (C) Size sorting of fluorescent microbeads FB-21, FB-205, FB-375 for miR-21, miR-205, miR-375 quantifications and machine-learning algorithm-assisted lung cancer diagnosis with subtypes classifications for 108 candidates serum samples.

Taking advantage of its highly permeable and nonfouling properties,[28,29] here we develop size-coded poly(ethylene glycol) (PEG) hydrogel microbeads for extraction-free quantification of three lung cancer highly expressed miRNAs (miR-205, miR-21, miR-375) from 108 serum samples including patients and healthy controls and achieved lung cancer diagnosis with major subtypes (AC, SCC, SCLC) classification via machine-learning algorithm-assisted data analysis. Three kinds of size-coded hydrogel microdroplets are synthesized via adjusting velocities of the continuous phase and dispersed phase of a microfluid. The dispersed phase contains PEG-diacrylate (PEG-DA), photoinitiator, and acrydite-modified nucleic acid capture probes for miR-21 (CP-21), miR-205 (CP-205), and miR-375 (CP-375), respectively. UV exposure is then performed for PEG-DA polymerization to solidify hydrogel microdroplets to hydrogel microbeads (MB-21, MB-205, MB-375) with uniform sizes of 14 μm, 19, and 27 μm, respectively (Scheme 1A). The as-prepared size-coded microbeads are directly mixed with candidates' serums without miRNA extraction pretreatment. Corresponding target miRNAs diffuse into hydrogel microbeads and are retained inside by hybridization with capture probes, while nonspecific miRNAs and protein in serum freely diffuse out of the hydrogel microbeads. Rolling circle amplification (RCA) reaction is then performed inside size-coded microbeads for miRNA signal amplification, and TAMRA-labeled reporter DNA (RE-TAM) is hybridized to as-obtained RCA product in hydrogel microbeads, which turns them to fluorescent microbeads (FB-21, FB-205, FB-375) (Scheme 1B). The three-dimensional network in hydrogel microbeads enhances loading capacities of capture probes and provides an appropriate aqueous reaction environment for subsequent DNA signal amplification reaction. More importantly, the porous and nonfouling hydrogel allows efficient retention of high-affinity target miRNA and fast removal of nonspecific ones, which achieves direct miRNA quantification from serum free of pre-extraction step. The as-obtained FB-21, FB-205, and FB-375 are sorted via flow cytometry and clustered into three groups in a forward scatter (FSC) - side scatter (SCC) plot according to their sizes. The corresponding

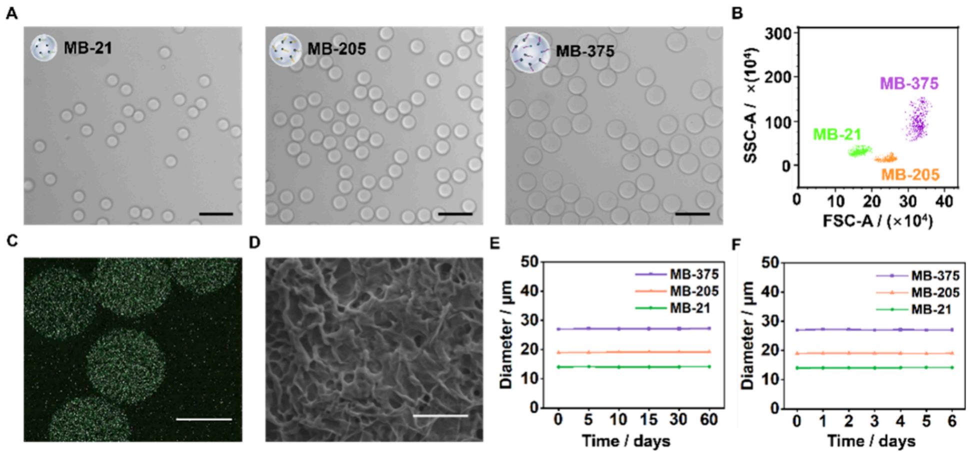

Figure 1. (A) Microphotographs and (B) flow cytometry FSC-SSC scatter graph for hydrogel microbeads MB-21, MB-205, and MB-375 (scale bar: 50 μm). (C) Fluorescence images of MB-21-FAM that synthesized with PEG-DA and CP-21-FAM (scale bar: 10 μm). (D) Scanning electronic microscopy image of hydrogel microbeads MB-21 (scale bar: 1 μm). Size of MB-21, MB-205, MB-375 stored in (E) TE buffer for 60 days and (F) serum for 6 days. The data error bars in (E,F) were collected from hydrogel microbeads from 3 different experiments and indicated as means ± SD.

TAMRA intensities for all three groups are calculated for miR-21, miR-205, and miR-375 quantifications. Principal component analysis (PCA) is then performed to evaluate the accuracy for lung cancer diagnosis with the establishment of a predictive model for lung cancer subtypes AC, SCC, and SCLC classifications (Scheme 1C).

SYNTHESIS OF SIZE-CODED HYDROGEL MICROBEADS

Hydrogel microbeads were synthesized via a home-built microfluidic system including a microfluidic chip, a FLOW-EZ pump, and a microscope equipped with a high-speed camera (Figure S1). The microfluidic chip consisted of two dispersed-phase inlets and one continuous-phase inlet (Figure S2A). The effect of both shear force and pressure at the junction of the dispersed phase and continuous phase sheared the flow into microdroplets (Figure S2B) and polymerized to stable hydrogel microbeads under 50 s UV irradiation. Successful polymerization of hydrogel microbeads was confirmed by the disappearance of PEG-DA -C═C- characteristic absorbance peak at 1635 $\mathrm{cm^{-1}}$ for hydrogel microbeads in FTIR absorption spectra (Figure S3). The velocity ratios between the dispersed phase and continuous phase determined the size and uniformity of microfluidic droplets and corresponding microbeads. As demonstrated in Figure S2C, the larger the velocity ratios of dispersed phase to continuous phase, the smaller the diameters of as-obtained hydrogel microbeads. The size-coded hydrogel microbeads MB-21, MB-205, and MB-375 were obtained as 14 ± 0.7 μm, 19 ± 0.9 μm, and 27 ± 1.4 μm, respectively (Figure 1A, Figure S2D). The FSC intensity of the hydrogel microbeads on flow cytometry was proportional to their size (Figure S4), which clustered the size-coded hydrogel microbeads into separated groups on the FSC-SSC scatter graph (Figure 1B). As indicated by the FSC histogram, hydrogel microbeads with size difference over 5 μm could be clearly distinguished in flow cytometry (Figure S5). These results indicated the capability of as-obtained hydrogel microbeads MB-21, MB-205, MB-375 for size corresponding sorting.

To confirm the immobilization of miRNA capture probe in hydrogel microbeads, CP-21 was labeled with fluorescein amidites (FAM) (CP-21-FAM) and copolymerized with PEG hydrogel precursor, which demonstrated uniform distribution of FAM fluorescence inside as-obtained MB-21-FAM (Figure 1C). The as-obtained hydrogel microbeads showed a porous structure with pore size ranging from 100 to 500 nm (Figure 1D), which allowed the free diffusion of target miRNAs into hydrogel scaffold and guaranteed sufficient proceeding of subsequent RCA reaction for signal amplification. The as-obtained hydrogel microbeads maintain stable size over 60 days of incubation in TE buffer (Figure 1E) and 6 days of incubation in serum (Figure 1F).

MiRNA SIGNAL AMPLIFICATION IN HYDROGEL MICROBEADS

To perform the as-obtained hydrogel microbeads for target miRNA signal amplification, they were incubated with TE buffer containing target miRNA. Take miR-21, for example, it was retained in MB-21 by hybridizing with CP-21 (Figure 2A, miR-21 recognition). The as-obtained duplex DNA strand was then annealed with a universal linker strand (UL) via T4 DNA ligase. The UL contained a circular template anchoring region, and RCA was subsequently performed in MB-21. RE-TAM was then incubated with MB-21 and hybridized to the as-obtained RCA product, which illuminated MB-21 for fluorescence signal amplification of miR-21 (Figure 2A, signal amplification).

The feasibility of RCA-based signal amplification was first verified by PAGE analysis. The circular template was transformed from ssDNA circligase and showed a new band with higher mobility than the linear DNA strand (Figure S6A). Taking miR-21 as a detection target, for example, hybridization of miR-21 to CP-21 resulted in a new band with lower mobility (Figure 2B, lane IV). Continuous incubation with the UL strand further decreased product mobility, which was accompanied by the disappearance of the CP-21/miR-21 hybridized band (Figure 2B, lane V). The as-obtained CP-21/miR-21/UL trihybridized complex was then hybridized with the circular template to active RCA reaction and generated RCA product with lowest mobility (Figure 2B, lane VII). On the contrary, CP-21 did not hybridize to the UL strand in the absence of miR-21; therefore, mixing CP-21 and UL resulted in their individual bands (Figure S6B). The successful coupling of miR-205 to CP-205 and miR-375 to CP-375 with

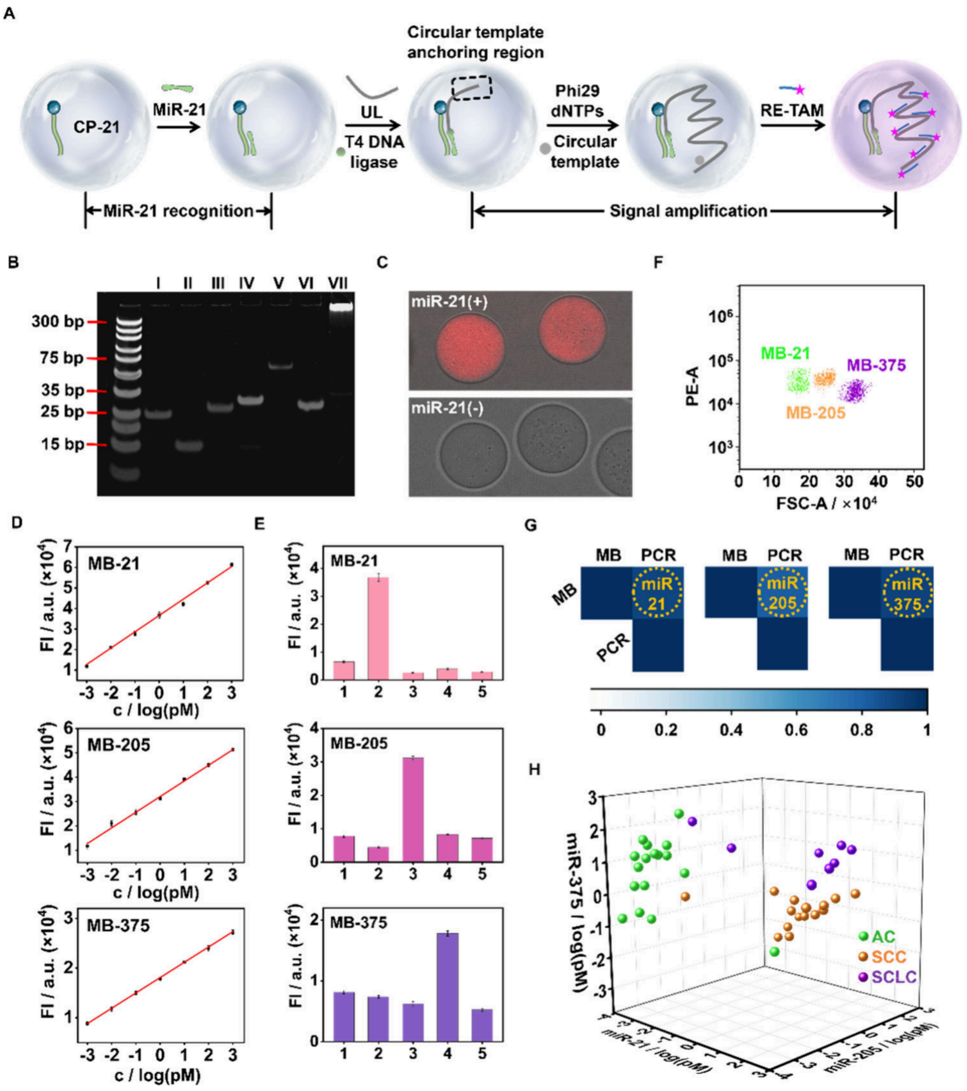

Figure 2. (A) Schematic illustration of the miR-21 fluorescence signal amplification process in MB-21. (B) PAGE verification of RCA reaction for miR-21. Lane I−VII represented CP-21, miR-21, UL, CP-21/miR-21 hybrid, CP-21/miR-21/UL trihybridized complex, cicular template, RCA product, respectively. (C) Fluorescence images of MB-21 after RCA reaction and RE-TAM coupling in the presence (miR-21(+)) and absence of miR-21 (miR-21(−)). (D) Linear relationship of TAMRA fluorescence intensity collected from MB-21, MB-205, MB-375 versus concentration of miR-21, miR-205, and miR-375, respectively. (E) TAMRA fluorescence intensity of MB-21, MB-205, MB-375 in response to (1) TE buffer, (2) 1 pM miR-21, (3) 1 pM miR-205, (4) 1 pM miR-375, and (5) 1 pM 1-base mismatched corresponding miRNA. The data error bars in (D) and (E) were collected from hydrogel microbeads from 3 different experiments and indicated as means ± SD. (F) FSC-PE scatter graph of MB-21, MB-205, and MB-375 corresponding to 1 pM of miR-21, miR-205, and miR-375, respectively. (G) Spearman's rank correlation coefficient for miR-21, miR-205, and miR-375 quantifications via hydrogel microbeads (MB) and qRT-PCR. The dashed line circled squares indicated the correlation between two different quantification methods. (H) Three-dimensional scatter profile of miR-21, miR-205, and miR-375 from 40 patients' serum samples including SCLC, AC, and SCC.

corresponding RCA reactions was also verified by PAGE (Figure S7A,B).

To visualize the RCA reaction in hydrogel microbeads, 100 pM miR-21 was incubated with MB-21 followed by the RCA reaction, which illuminated the whole hydrogel microbead with strong TAMRA fluorescence (Figure 2C, miR-21 (+)), indicating the capability for miRNA quantification via flow cytometry. In comparison, signal amplification was also performed for MB-21 that was also incubated with UL but in the absence of miR-21, which barely showed TAMRA fluorescence (Figure 2C, miR-21 (−)). To verify the quantification capability, MB-21 was incubated with different concentrations of miR-21 followed by RCA reaction in beads. The as-treated MB-21 was collected and analyzed with flow cytometry, and the corresponding TAMRA fluorescence intensity was determined by integrating PE channel fluorescence intensity for all the illuminated MB-21, which demonstrated a linear relationship corresponding to miR-21 concentration from 1 fM to 1 nM with limit of detection (LOD) of 0.2 fM (Figure 2D, MB-21). MB-205 and MB-375 demonstrated the same detection linear ranges corresponding to miR-205 and miR-375, with LOD of 0.5 and 0.1 fM, respectively (Figure 2D, MB-205, MB-375). The as-achieved LODs were slightly superior than currently reported fluorescent detection approaches[30−33] and qualified for direct miRNA quantification from serum. The reaction specificity indicated the efficient capture of target miRNA by the corresponding hydrogel microbead with little nonspecific

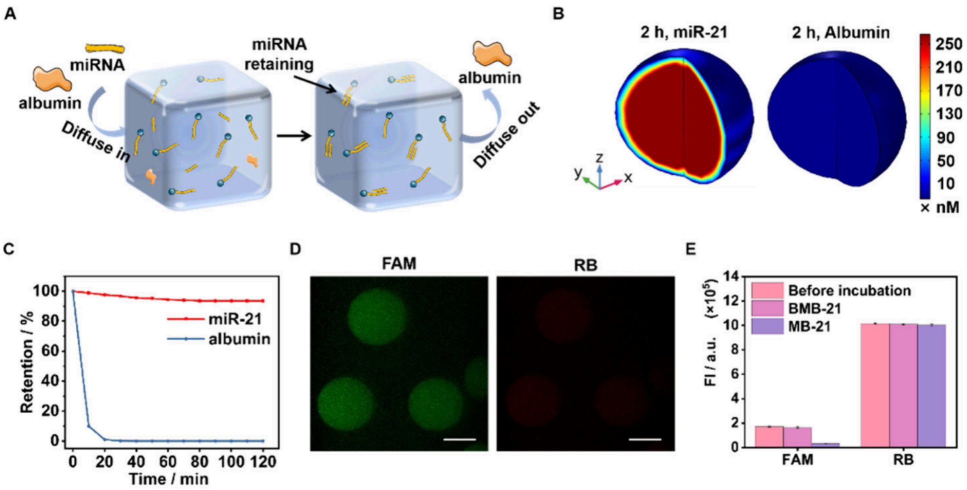

Figure 3. (A) Schematic illustration of hydrogel microbeads retaining target miRNA while preventing serum component fouling. (B) A diffusion-binding model of miR-21 and albumin distributions in MB-21 after 2 h incubation and (C) corresponding retention percentages according to time. The color change in (B) represented different target concentrations at different positions inside hydrogel microbeads. (D) Z-stack picture of MB-21 incubated with FAM-miR-21 and RB-Albumin (scale bar: 10 μm). (E) FAM and RB intensities for 10 nM FAM-miR-21 and 0.2 mg/mL RB-albumin (Before incubation) and the corresponding fluorescence of supernatant solutions after they incubated with MB-21 and BMB-21.

beads retained (Figure S8). In addition, MB-21, MB-205, and MB-375 were also incubated with 1 pM miR-21, miR-205, miR-375, and 1 base mismatched miR-21, respectively, which only showed TAMRA fluorescence to corresponding target miRNA with little fluorescence from nonspecific targets (Figure 2E). These results indicated good reaction specificity with little cross reaction among three different kinds of miRNAs.

VERIFICATION OF THE CAPABILITY OF HYDROGEL MICROBEADS FOR CANCER SUBTYPE DISCRIMINATION

To evaluate the capability of size-coded hydrogel microbeads for different kinds of miRNAs classification and quantification, 1 pM of miR-21, miR-205, and miR-375 mixtures was mixed with MB-21, MB-205, and MB-375. After RCA reaction and RE-TAM strand coupling to illuminate hydrogel microbeads, the as-obtained microbeads mixture were sorted into three different groups according to their size via flow cytometry (Figure 2F). The total TAMRA fluorescence intensities from each group were evaluated by integrating corresponding PE channel fluorescence intensity for illuminated MB-21, MB-205, and MB-375, respectively. To evaluate quantification accuracy, miRNAs were extracted from 9 serum samples and quantified with size-coded hydrogel microbeads. The quantification results were further compared to qRT-PCR results (Figure S9, Table S2). Spearman's correlation coefficients of two quantification methods were obtained as 0.90, 0.78, and 0.89, respectively, for miR-21, miR-205, and miR-375 (Figure 2G), which confirmed size-coded hydrogel microbeads as a reliable miRNA quantification strategy.

The capability of hydrogel microbeads for cancer subtype classification was then verified with serum samples of 40 patients including 15 SCC, 17 AC, and 8 SCLC. MiR-21, miR-205, and miR-375 were extracted and quantified via size-coded hydrogel microbeads (Table S3), and their distributions demonstrated obvious aggregation tendency within lung cancer subtypes in a three-dimensional scatter diagram (Figure 2H) and the corresponding two-dimensional plane based on t-SNE analysis (Figure S10). These results indicated the capability of size-coded hydrogel microbeads for serum miRNAs expression quantification and corresponding lung cancer subtype classification.

VERIFICATION OF ANTIFOULING CAPABILITY OF HYDROGEL MICROBEADS IN SERUM

Taking advantage of the nonfouling capability of hydrogel microbeads, here we achieved extraction-free multi-miRNAs quantification directly from patients' serum. The as-prepared hydrogel microbeads provided an environment which allowed free diffusion of target miRNA and efficient proceeding of RCA in the hydrogel scaffold. Nonspecific proteins and macromolecules that highly existed in serum, such as albumin, have low-affinity to hydrogel, thus were quickly removed from hydrogel[34,35] and, therefore, would not affect miRNA quantifications (Figure 3A).

The binding affinities and the corresponding dissociation constants (KDs) of CP-21 to miR-21 and albumin (example of nonspecific serum protein) were measured as 140 pM and 3 μM, respectively (Figure S11), which indicated efficient retention capability of MB-21 for miR-21 with good non-fouling capability to nonspecific serum proteins. A diffusion-binding model was further established via COMSOL (Table S4) to evaluate the retention probabilities of miR-21 and albumin in MB-21 by assuming that miR-21 and albumin were initially freely distributed in a whole hydrogel microbead. After 2 h incubation, miR-21 showed high concentration in hydrogel microbeads, indicating its efficient retaining, while albumin completely diffused out of hydrogel microbeads (Figure 3B), indicating good nonfouling capability of hydrogel microbeads. The time corresponding retention percentages of miR-21 and albumin in MB-21 were calculated by calculating time corresponding miR-21 and albumin concentration change in hydrogel microbeads and obtained 93.6% for miR-21 after 2 h incubation. On the contrary, albumin retention percentage in MB-21 quickly decreased to 0.01% in the first 20 min of incubation (Figure 3C).

To further visualize different retention capabilities of miR-21 and albumin in hydrogel microbeads, MB-21 was incubated with 10 nM FAM-labeled miR-21 (FAM-miR-21) and various

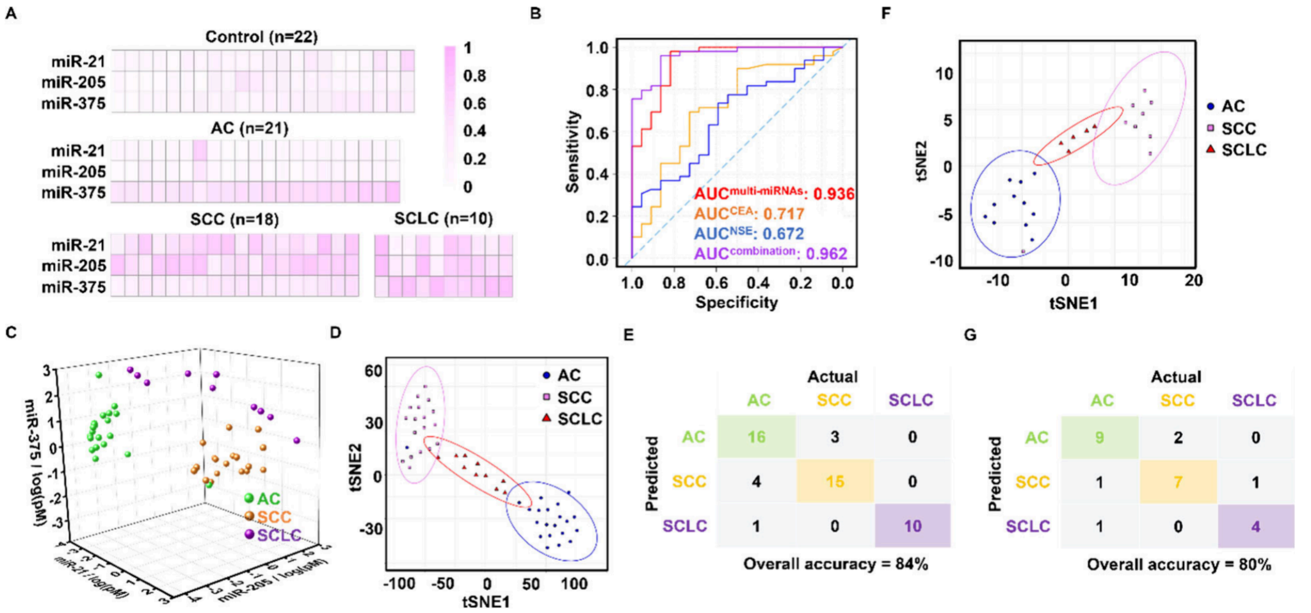

Figure 4. (A) Heatmap of the expression levels of miR-21, miR-205, and miR-375 from 71 serum samples including healthy control and AC, SCC, and SCLC patients in training cohort. (B) ROC curves of multi-miRNAs panel (red), CEA (orange), NSE (blue), combination of multi-miRNAs, CEA, and NSE (purple) for lung cancer diagnosis. (C) Three-dimensional scatter profile and (D) corresponding t-SNE analysis of miR-21, miR-205, and miR-375 from 49 serum samples including AC, SCC, and SCLC patients in training cohort. Consistency of predictive model and actual situation for subtype discrimination in (E) training cohort and (G) validation cohort. (F) t-SNE analysis of miR-21, miR-205, and miR-375 from 25 serum samples including AC, SCC, and SCLC patients in validation cohort.

concentrations of Rhodamine B (RB)-labeled albumin (RB-albumin) from 0.05 to 0.2 mg/mL for 2 h. Z-stack imaging of MB-21 demonstrated uniform FAM fluorescence distribution through the whole microbead but little RB fluorescence (Figure 3D). In addition, the supernatant of incubation solution was collected, which demonstrated a similar intensity of RB before and after incubation (Figure S12A, Figure 3E, RB). RB-albumin concentrations in the supernatant were quantified via a protein assay kit, which demonstrated a negligible absorbance decrease after incubating with MB-21 (Figure S13B), indicating the complete removal of albumin from hydrogel microbeads. On the contrary, FAM fluorescence in supernatant demonstrated 82% decrease after incubating with MB-21 (Figure S12B, Figure 3E, FAM), indicating efficient retainment of miR-21 in hydrogel microbeads. As a control, bare hydrogel microbeads-21 (BMB-21) that were prepared in the absence of CP-21 were also incubated with 10 nM FAM-miR-21 and 0.2 mg/mL RB-albumin for 2 h, which showed similar FAM and RB fluorescence intensities in the supernatant before and after incubation (Figure S12, Figure 3E, BMB-21). These results confirmed the antifouling capability of hydrogel microbeads with efficient and specific retention of corresponding target miRNA.

To further evaluate the interference of serum biological components to the accuracy of microbead-based miRNA quantification, series concentrations of miR-21, miR-205, and miR-375 were spiked in 5 mg/mL BSA, and the miRNA-containing BSA solution were incubated with MB-21, MB-205, and MB-375 followed by RCA signal amplification and RE-TAM hybridization. It achieved similar signal intensities and linear ranges for miR-21, miR-205, and miR-375 quantifications in BSA (Figure S14) compared with their quantifications in buffer (Figure 2D). Furthermore, 1, 5, and 10 pM standard solutions of miR-375 were spiked into healthy people serum samples, respectively, and quantified via hydrogel microbeads. The corresponding concentrations were compared with spiked concentrations to obtain recovery rates of 107.2% for 1 pM, 101.9% for 5 pM, and 104.0% for 10 pM miR-375, respectively (Table S5). These results all indicated the feasibility of hydrogel microbeads for extraction-free miRNA detection directly from serum.

EXTRACTION-FREE MULTI-miRNAs DETECTION FROM SERUM FOR LUNG CANCER SUBTYPE DIAGNOSIS

108 blood serum samples including AC, SCC, and SCLC patients and healthy controls (Table S6) were directly mixed with hydrogel microbeads of MB-21, MB-205, and MB-375 without pre-extraction, and miRNA expression levels were quantified via flow cytometry. The training cohort of 71 serum samples including patients of lung cancer subtypes AC ($n = 21$), SCC ($n = 18$), and SCLC ($n = 10$) and healthy control ($n = 22$) was established, and the relative expression levels of miR-21, miR-205, and miR-375 were shown in the heatmap (Figure 4A) and box-plot (Figure S15). A panel of multi-miRNAs levels was constructed in a receiver operating characteristic (ROC) curve and showed an excellent performance for identifying lung cancer patients with an AUC of 0.936, which was much higher compared with the AUC for only one type of miRNA (Figure S16, Table S7, training cohort). The expression levels of normal lung cancer biomarkers, carcinoembryonic antigen (CEA), and neuron-specific enolase (NSE) for the 71 serum samples were also analyzed and obtained AUC of 0.717 and 0.672, respectively. The combination of the multi-miRNAs panel, CEA, and NSE highly improved the AUC to 0.962 (Figure 4B, Table S7). These results indicated the superiority of quantification of multi-miRNAs expression levels for lung cancer diagnosis.

For lung cancer subtype discrimination, the three-dimensional scatter diagram of miR-21, miR-205, and miR-375 expression distributions for 49 lung cancer serum samples in the training cohort was pictured, which demonstrated obvious aggregation tendency within lung cancer subtypes (Figure 4C). The classification results were visualized onto a two-dimensional plane, demonstrating an obvious aggregation tendency within lung cancer subtypes (Figure 4D). The classification accuracy was determined by comparing classification results predicted by our model with pathological results and obtained 84% consistency (Figure 4E).

An independent validation cohort of 37 serum samples including patients of AC (n = 11), SCC (n = 9), and SCLC (n = 5) and healthy control (n = 12) was then established to evaluate the performance of size-coded hydrogel microbeads for lung cancer diagnosis and subtype discrimination. MiR-21, miR-205, and miR-375 expression levels were directly quantified from serum samples via hydrogel microbeads (Figure S17A). The ROC curve showed an AUC of 0.930 for lung cancer diagnosis for the multi-miRNAs panel, which was much higher compared with AUC for CEA (0.643), NSE (0.778). The combination of the multi-miRNAs panel, CEA, and NSE highly improved the AUC to 0.943 (Figure S17B, Table S7). The three-dimensional scatter diagram of all three miRNAs expression distributions for 25 serum samples in the validation cohort including AC, SCC, and SCLC (Figure S18) and the corresponding two-dimensional plane (Figure 4F) also demonstrated an obvious aggregation tendency within subtypes. The lung cancer subtype prediction accuracy was determined as 80% consistent by comparing with pathological results (Figure 4G). These results indicated the great clinical application prospect of these miRNAs for diagnosing lung cancer subtypes and could be conveniently extended as a universal approach for cancer subtype discrimination.

In summary, an extraction-free quantification method for serum multi-miRNAs using size-coded hydrogel microbeads was developed. We detected the expression levels of miR-21, miR-205, and miR-375 from candidates' serum, demonstrating an accurate and reliable result for classifying different subtypes of lung cancer with the aid of machine learning. With the convenience for microbead size adjustment and conjugation of different fluorescent dyes as detection signal channels, the as-reported method showed a good scalability capability. With the application of capture antibody and detection antibody that coupled with DNA strand containing circular template, the detection targets could also be extended from miRNAs to protein biomarkers. The method developed in this study shows considerable potential for biomarker quantification and helps to broaden the development prospect of noninvasive cancer evaluation methods.

■ ASSOCIATED CONTENT

Supporting Information

The Supporting Information is available free of charge at https://pubs.acs.org/doi/10.1021/acs.nanolett.4c05233.

> Materials, synthesis and characterization for hydrogel microbeads, detailed procedures of serum miRNAs quantification, Figures S1–S17, Tables S1–S7 (PDF)

■ AUTHOR INFORMATION

Corresponding Authors

Feng Yan – *The Affiliated Cancer Hospital of Nanjing Medical University, Jiangsu cancer hospital, Jiangsu Institute of cancer research, Nanjing 210009, China*;
Email: yanfeng@jszlyy.com.cn

Ying Liu – *State Key Laboratory of Analytical Chemistry for Life Science, School of Chemistry and Chemical Engineering, Nanjing University, Nanjing 210023, China; Chemistry and Biomedicine Innovation Center, Nanjing University, Nanjing 210023, China*; orcid.org/0000-0001-5718-7804;
Email: yingliu@nju.edu.cn

Authors

Dayu Chen – *The Affiliated Cancer Hospital of Nanjing Medical University, Jiangsu cancer hospital, Jiangsu Institute of cancer research, Nanjing 210009, China*

Yingfei Wang – *State Key Laboratory of Analytical Chemistry for Life Science, School of Chemistry and Chemical Engineering, Nanjing University, Nanjing 210023, China; State Key Laboratory of Digital Medical Engineering, School of Biological Science and Medical Engineering, Southeast University, Nanjing 210096, China*

Ying Wei – *College of Engineering and Applied Science, Nanjing University, Nanjing 210023, China*

Zhenda Lu – *College of Engineering and Applied Science, Nanjing University, Nanjing 210023, China*; orcid.org/0000-0002-9616-8814

Huangxian Ju – *State Key Laboratory of Analytical Chemistry for Life Science, School of Chemistry and Chemical Engineering, Nanjing University, Nanjing 210023, China*; orcid.org/0000-0002-6741-5302

Complete contact information is available at:
https://pubs.acs.org/10.1021/acs.nanolett.4c05233

Author Contributions

[#](D.C., Y.W.) These authors contributed equally to this work. D.C designed and performed the experiments parts. Y.W assisted with generating hydrogel microbeads. Y.W and Z.L assisted with model simulations. H.J, F.Y provided advice for the experiment. D.C wrote the manuscript. Y.L supervised the study and revised the manuscript. All authors have given approval to the final version of the manuscript.

Notes

The authors declare no competing financial interest.

■ ACKNOWLEDGMENTS

We are deeply acknowledge the National Natural Science Foundation of China (22374073, 22404019), the Cutting-edge Technology Research and Development Program of Jiangsu Province (BF2024055), Jiangsu Funding Program for Excellent Postdoctoral Talent (2024ZB081), the Postdoctoral Fellowship Program of CPSF (GZC20240249), and State Key Laboratory of Analytical Chemistry for Life Science (SKLACLS2413).

■ REFERENCES

(1) Sung, H.; Ferlay, J.; Siegel, R. L.; et al. Global Cancer Statistics 2020: GLOBOCAN Estimates of Incidence and Mortality Worldwide for 36 Cancers in 185 Countries. *CA Cancer J. Clin* **2021**, *71* (3), 209–2493.

(2) Thai, A. A.; Solomon, B. J.; Sequist, L. V.; Gainor, J. F.; Heist, R. S. Lung cancer. *Lancet* **2021**, *398*, 535–554.

(3) Howlader, N.; Forjaz, G.; Mooradian, M. J.; et al. The Effect of Advances in Lung-Cancer Treatment on Population Mortality. *N Engl J. Med.* **2020**, *383*, 640–649.

(4) Siegel, R. L.; Miller, K. D.; Wagle, N. S.; Jemal, A. Cancer statistics, 2023. *CA Cancer J. Clin* **2023**, *73*, 17−48.

(5) Travis, W. D.; Brambilla, E.; Nicholson, A. G.; et al. The 2015 World Health Organization Classification of Lung Tumors: Impact of Genetic, Clinical and Radiologic Advances Since the 2004 Classification. *J. Thorac Oncol* **2015**, *10* (9), 1243−1260.

(6) Yatabe, Y.; Dacic, S.; Borczuk, A. C.; et al. Best Practices Recommendations for Diagnostic Immunohistochemistry in Lung Cancer. *J. Thorac Oncol* **2019**, *14*, 377−407.

(7) Ignatiadis, M.; Sledge, G. W.; Jeffrey, S. S. Liquid biopsy enters the clinic - implementation issues and future challenges. *Nat. Rev. Clin Oncol* **2021**, *18* (5), 297−312.

(8) Wang, C.; Xie, Y.; Song, X.; et al. A NIR Programmable In Vivo miRNA Magnifier for NIR-II Imaging of Early Stage Cancer. *Angew. Chem., Int. Ed. Engl.* **2023**, *62* (50), No. e202312665.

(9) Dong, H.; Lei, J.; Ding, L.; Wen, Y.; Ju, H.; Zhang, X. MicroRNA: function, detection, and bioanalysis. *Chem. Rev.* **2013**, *113* (8), 6207−6233.

(10) Li, J. H.; Sun, S. S.; Li, N.; Lv, P.; Xie, S. Y.; Wang, P. Y. MiR-205 as a promising biomarker in the diagnosis and prognosis of lung cancer. *Oncotarget* **2017**, *8*, 91938−91949.

(11) Sromek, M.; Glogowski, M.; Chechlinska, M.; et al. Changes in plasma miR-9, miR-16, miR-205 and miR-486 levels after non-small cell lung cancer resection. *Cell Oncol (Dordr* **2017**, *40*, 529−536.

(12) Zaporozhchenko, I. A.; Morozkin, E. S.; Skvortsova, T. E.; et al. Plasma miR-19b and miR-183 as Potential Biomarkers of Lung Cancer. *PLoS One* **2016**, *11*, No. e0165261.

(13) Charkiewicz, R.; Pilz, L.; Sulewska, A.; et al. Validation for histology-driven diagnosis in non-small cell lung cancer using hsa-miR-205 and hsa-miR-21 expression by two different normalization strategies. *Int. J. Cancer* **2016**, *138*, 689−697.

(14) Mao, S.; Zheng, S.; Lu, Z.; et al. Exosomal miR-375−3p breaks vascular barrier and promotes small cell lung cancer metastasis by targeting claudin-1. *Transl Lung Cancer Res.* **2021**, *10*, 3155−3172.

(15) Petkova, V.; Marinova, D.; Kyurkchiyan, S.; et al. MiRNA expression profiling in adenocarcinoma and squamous cell lung carcinoma reveals both common and specific deregulated microRNAs. *Medicine (Baltimore)* **2022**, *101*, No. e30027.

(16) Saviana, M.; Romano, G.; McElroy, J.; et al. A plasma miRNA-based classifier for small cell lung cancer diagnosis. *Front Oncol* **2023**, *13*, No. 1255527.

(17) Jet, T.; Gines, G.; Rondelez, Y.; Taly, V. Advances in multiplexed techniques for the detection and quantification of microRNAs. *Chem. Soc. Rev.* **2021**, *50* (6), 4141−4161.

(18) Mitchell, P. S.; Parkin, R. K.; Kroh, E. M.; et al. Circulating microRNAs as stable blood-based markers for cancer detection. *Proc. Natl. Acad. Sci. U. S. A.* **2008**, *105* (30), 10513−10518.

(19) Williams, Z.; Ben-Dov, I. Z.; Elias, R.; et al. Comprehensive profiling of circulating microRNA via small RNA sequencing of cDNA libraries reveals biomarker potential and limitations. *Proc. Natl. Acad. Sci. U. S. A.* **2013**, *110* (11), 4255−4260.

(20) Roy, S.; Soh, J. H.; Ying, J. Y. A microarray platform for detecting disease-specific circulating miRNA in human serum. *Biosens Bioelectron* **2016**, *75*, 238−246.

(21) Wu, Z.; Zheng, Y.; Lin, L.; Mao, S.; Li, Z.; Lin, J. M. Controllable Synthesis of Multicompartmental Particles Using 3D Microfluidics. *Angew. Chem., Int. Ed. Engl.* **2020**, *59*, 2225−2229.

(22) Wu, J.; Lin, Z.; Zou, Z.; et al. Identifying the Phenotypes of Tumor-Derived Extracellular Vesicles Using Size-Coded Affinity Microbeads. *J. Am. Chem. Soc.* **2022**, *144* (51), 23483−23491.

(23) Yang, Q.; Lin, J.; Liu, M.; et al. Highly sensitive sequencing reveals dynamic modifications and activities of small RNAs in mouse oocytes and early embryos. *Sci. Adv.* **2016**, *2* (6), No. e1501482.

(24) Cheng, J.; Swarup, N.; Li, F.; et al. Distinct Features of Plasma Ultrashort Single-Stranded Cell-Free DNA as Biomarkers for Lung Cancer Detection. *Clin Chem.* **2023**, *69* (11), 1270−1282.

(25) Cai, S.; Pataillot-Meakin, T.; Shibakawa, A.; et al. Single-molecule amplification-free multiplexed detection of circulating microRNA cancer biomarkers from serum. *Nat. Commun.* **2021**, *12* (1), 3515.

(26) Bidarra, D.; Constâncio, V.; Barros-Silva, D.; et al. Circulating MicroRNAs as Biomarkers for Prostate Cancer Detection and Metastasis Development Prediction. *Front Oncol* **2019**, *9*, 900.

(27) McDonald, J. S.; Milosevic, D.; Reddi, H. V.; Grebe, S. K.; Algeciras-Schimnich, A. Analysis of circulating microRNA: preanalytical and analytical challenges. *Clin Chem.* **2011**, *57* (6), 833−840.

(28) Li, S.; Dai, J.; Zhu, M.; et al. Implantable Hydrogel-Protective DNA Aptamer-Based Sensor Supports Accurate, Continuous Electrochemical Analysis of Drugs at Multiple Sites in Living Rats. *ACS Nano* **2023**, *17* (18), 18525−18538.

(29) Singh, N. K.; Wang, Y.; Wen, C.; et al. High-affinity one-step aptamer selection using a non-fouling porous hydrogel. *Nat. Biotechnol.* **2024**, *42* (8), 1224−1231.

(30) Chen, Y.; Wang, X.; Zhang, J.; et al. Split crRNA with CRISPR-Cas12a enabling highly sensitive and multiplexed detection of RNA and DNA. *Nat. Commun.* **2024**, *15* (1), 8342.

(31) Song, C.; Liu, C.; Chen, J.; et al. Self-Generation of Distinguishable Fluorescent Probes via a One-Pot Process for Multiple MicroRNA Detection by Liquid Chromatography. *Anal. Chem.* **2023**, *95* (8), 4113−4121.

(32) Zhang, P.; Tong, Y.; Huang, X.; et al. The Dual-Response-Single-Amplification Fluorescent Nanomachine for Tumor Imaging and Gastric Cancer Diagnosis. *ACS Nano* **2023**, *17* (17), 16553−16564.

(33) Zhao, S.; Zhang, S.; Hu, H.; et al. Selective In Situ Analysis of Mature microRNAs in Extracellular Vesicles Using a DNA Cage-Based Thermophoretic Assay. *Angew. Chem., Int. Ed. Engl.* **2023**, *62* (24), No. e202303121.

(34) Chan, D.; Chien, J. C.; Axpe, E.; et al. Combinatorial Polyacrylamide Hydrogels for Preventing Biofouling on Implantable Biosensors. *Adv. Mater.* **2022**, *34* (24), No. e2109764.

(35) Yuan, J.; Sun, Y.; Wang, K.; et al. Development and validation of reassigned CEA, CYFRA21−1 and NSE-based models for lung cancer diagnosis and prognosis prediction. *BMC Cancer* **2022**, *22* (1), 686.